

## Article

# Statistical Study of Equatorial Ionospheric Anomaly after Midnight Based on FY-3(D) Ionospheric Photometer

Bin Zhang<sup>1,2,3,4</sup>, Liping Fu<sup>1,3,4,\*</sup>, Tian Mao<sup>5,6,\*</sup>, Xiuqing Hu<sup>5,6</sup>, Fang Jiang<sup>1,3,4</sup>, Nan Jia<sup>1,2,3,4</sup>, Tianfang Wang<sup>1,2,3,4</sup>, Ruyi Peng<sup>1,3,4</sup> and Jinsong Wang<sup>5,6</sup>

<sup>1</sup> National Space Science Center, Chinese Academy of Sciences, Beijing 100190, China

<sup>2</sup> University of Chinese Academy of Sciences, Beijing 100190, China

<sup>3</sup> Beijing Key Laboratory of Space Environment Exploration, Beijing 100190, China

<sup>4</sup> Key Laboratory of Environmental Space Situation Awareness Technology, Beijing 100190, China

<sup>5</sup> Key Laboratory of Space Weather, National Satellite Meteorological Center (National Center for Space Weather), Beijing 100081, China

<sup>6</sup> Innovation Center for FengYun Meteorological Satellite (FYSIC), Beijing 100081, China

\* Correspondence: fuliping@nssc.ac.cn (L.F.); maotian@cma.gov.cn (T.M.); Tel.: +86-136-4121-2972 (L.F.); +86-136-1115-4091(T.M.)

**Abstract:** The OI135.6 nm radiation intensity and the associated change with solar activity are very complex, and this is particularly the case during November 2020. In this paper, we investigated the OI135.6 nm radiation intensity in the low-latitude ionosphere during a quiet geomagnetic period. The Ionospheric Photometer (IPM) instrument onboard the FY-3(D) meteorological satellite was employed to measure the OI135.6 nm night airglow at 02:00 LT (local time) and its response to the solar activity. The results showed there is a statistically significant correlation between the intensity of the equatorial ionospheric anomaly (EIA) and solar activity after midnight. The EIA at 02:00 LT and before midnight shared the same climatological characteristics—strong in equinoxes and weak in solstices. In November 2020, when the F10.7 flux significantly increased, the OI135.6 nm radiation intensity in the EIA region recorded a 100–200% increase compared to the previous month, which was much higher than in the same period in the preceding two years. A similar phenomenon was observed at the same time by the Global-scale Observations of Limb and Disk (GOLD), which makes continuous observations of ionospheric structure variation in global patterns. Data analysis suggests that the EIA at 02:00 LT was due to the attenuation of the EIA before midnight after the disappearance of the eastward electric field. The magnetic latitude of the EIA crest (hereafter denoted by  $\theta_{ml}F2$ ) indicates a range-and-seasonal rule of hemispherical asymmetry: closer to the geomagnetic equator in equinoxes and farther away from the geomagnetic equator in solstices. Further studies are needed.

**Keywords:** far ultraviolet nightglow; equatorial ionospheric anomaly; F10.7; FY-3(D)



**Citation:** Zhang, B.; Fu, L.; Mao, T.; Hu, X.; Jiang, F.; Jia, N.; Wang, T.; Peng, R.; Wang, J. Statistical Study of Equatorial Ionospheric Anomaly after Midnight Based on FY-3(D) Ionospheric Photometer. *Atmosphere* **2022**, *13*, 2068. <https://doi.org/10.3390/atmos13122068>

Academic Editors: Sergey Pulintsev and Alexei Dmitriev

Received: 3 November 2022

Accepted: 3 December 2022

Published: 9 December 2022

**Publisher's Note:** MDPI stays neutral with regard to jurisdictional claims in published maps and institutional affiliations.



**Copyright:** © 2022 by the authors. Licensee MDPI, Basel, Switzerland. This article is an open access article distributed under the terms and conditions of the Creative Commons Attribution (CC BY) license (<https://creativecommons.org/licenses/by/4.0/>).

## 1. Introduction

The equatorial ionization anomaly (EIA) in the ionospheric F-region has been extensively studied. The EIA is commonly believed to result from the fountain effect driven by the upward vertical  $E \times B$  plasma drift caused by the eastward zonal electric field  $E$  and the northward magnetic field  $B$  near the magnetic equator. As the plasma rises to higher altitudes, it spreads along the geomagnetic field lines on both sides of the magnetic equator due to pressure and gravity [1–3]. Finally, this plasma accumulates to form double crests on both sides of the magnetic equator and creates a plasma density valley around the magnetic equator [4,5]. At night, ionospheric  $O^+$  recombines with electrons or  $O^-$  producing excited atomic oxygen (OI). The 5s-3p transition of OI produces light with a wavelength of 135.6 nm, whose intensity is proportional to the square of the  $O^+$  concentration of oxygen ions [6]. Since oxygen ion  $O^+$  is the main component of the ionosphere, it can be approximated that the 135.6-nm band intensity is proportional to the square of

the electron density. The OI135.6-nm intensity obtained by optical detection can be used to study the ionospheric conditions at night.

Ionospheric EIA observation by optical instruments on satellites has good spatiotemporal continuity, compensating for the lack of ground-based stations on the ground and ocean. In the past few decades, the OI 135.6 nm emission observed by remote sensing has developed into the most widely used optical means for observing and quantifying ionospheric plasma parameters [7–18]. So far, the OI135.6 nm wavelength ionospheric emission has been used to study EIA features for many years [19–21]. In 2005, the four-wave longitudinal structure of the EIA crests was first reported by Sagawa [22]. Liu et al. used CHALLENGING Mini-satellite Payload (CHAMP) data to study the correlation between the EIA after midnight incidence and date, local time, solar activity, and longitude [23]. Kil et al. investigated the seasonal, longitudinal, and altitudinal variations of the F-region morphology at 21:00 to 23:00 LT in the low and middle latitudes using the Special Sensor Ultraviolet Spectrographic Imager (SSUSI) instrument on board the Defense Meteorological Satellite Program (DMSP) F15 and the Global Ultraviolet Imager (GUVI) on board the Thermosphere, Ionosphere, Mesosphere Energetics and Dynamics (TIMED) satellite data collected in August, September, and November of 2003. They inferred that the hemispheric asymmetry of the topside ionosphere is created primarily by the retardation of the downward plasma diffusion in one hemisphere through the field-aligned equatorward winds [24]. Henderson et al. found that, for all longitudes, the crest-to-trough ratio (CTR) was well correlated with the equatorial plasma bubble (EPB) rate, using GUVI 135.6 nm radiation from the 20:30 to 21:30 Magnetic Local Time [25]. Lin et al. used the Formosa Satellite 3 and Constellation Observing System for Meteorology, Ionosphere, and Climate (FORMOSAT-3/COSMIC or F3/C in short) satellite constellation radio occultation observations to monitor the development and subsidence of the four-wave longitudinal structure of the equatorial ionosphere during a 24 h local time period [26]. Lin et al. studied the EIA structures and evolutions using the radio occultation observation of the F3/C, which suggested that, in addition to the asymmetric neutral composition effect, interactions between the summer-to-winter (transequatorial) neutral winds and strength of the equatorial plasma fountain effect play important roles in producing the asymmetric development of the EIA crests [27].

Laskar et al. utilized the GOLD OI 135.6 nm data to study the morning EIA over the American continents. They attributed it to the four-wave structure in the early morning based on Whole Atmosphere Community Climate Model-eXtended (WACCM-X) simulations [28]. Cai et al. found an extra electron density (Ne) peak after sunset at approximately 30° S near 40° W on 4 November 2019, which is poleward and immediately next to the southern EIA crest. The Whole Atmosphere Community Climate Model-eXtended diagnostic analysis revealed that the decrease of Ne and hmF2 between 15° and 25° S made Ne near 30° S appear as an extra density peak relative to the southern EIA crest [29]. Cai et al. found a distinct post-sunset, hemispherically asymmetric evolution of the equatorial ionization anomaly between 40° and 50° W on 19 November 2018, with the southern crest shifting poleward but the northern crest remaining in the same latitude region, which was due to the hemispheric asymmetry in the plasma transport due to  $E \times B$  drifts and neutral winds [30].

Most studies about the ionosphere after midnight used data from ground-based observations, which are severely limited by the spatial distribution of ground-based stations. The optical remote sensing payload can observe the ionosphere after midnight at the middle and low latitudes in satellites, such as the FY-3(D) IPM and GOLD ultraviolet imaging spectrographs. Since the GOLD is located in a geostationary orbit, it can only observe half of the Earth because of the curvature of the Earth's surface. Jee used TOPEX/Poseidon radar data to study the climatological patterns of the TEC in solar cycles, geomagnetic activity, seasons, etc. They show strong TEC variations with solar activity but relatively weak variations with geomagnetic activity [31]. However, the TOPEX/Poseidon data only included the ocean and lacked land data. Most EIA studies, such as those on longitudinal

four-wave structure, focus on the daytime and before midnight since the EIA is too weak [32, 33]. Few EIA studies have used ground-based data after midnight and do not cover the globe. In satellite remote sensing observation, the ionosphere is weak and difficult to detect after midnight. In this paper, we studied the EIA structure after midnight based on the Feng Yun 3-D (FY-3D) Ionospheric Photometer (IPM) data.

## 2. Data and Methods

The compact and high-sensitivity nadir-viewing FUV Ionospheric Photometer (IPM) is one of 10 scientific payloads aboard the Feng Yun 3-D (FY-3D) meteorological satellite [34]. The orbit altitude of the FY-3D is 831 km, the inclination is  $98.753^\circ$ , the quasi-repeat time is 4–10 days, and the local time of the ascending node is 02:00/14:00. Moreover, with high optical sensitivity and spatial resolution, the IPM can effectively detect the weak ionosphere after midnight.

The IPM monitors nadir 135.6-nm emissions in the nightside thermosphere and 135.6 nm and N2 LBH emissions in the dayside thermosphere, and then the total ionospheric electron density (TEC), peak ionospheric electron density of the F2 layer ( $N_mF_2$ ), and thermospheric column density ratio of atomic oxygen to molecular nitrogen (O/N2) were retrieved [13,35,36]. The IPM parameters are shown in Table 1:

**Table 1.** FY-(3D) IPM instrument parameters.

Parameter	Value
Field of view	$\sim 3.5^\circ$ (along orbit) $\times$ $1.6^\circ$ (cross orbit)
Band of detection	night mode: 135.6 nm
	day mode: 135.6 nm and N2LBH
Sensitivity	day mode: N2LBH channel: 11 counts/s/Rayleigh
	135.6 nm channel: 8 counts/s/Rayleigh night mode:
	135.6-nm channel: 226 counts/s/Rayleigh
Bandwidth	135.6 nm@day mode: FWHM = 7.5-nm
	N2LBH@day mode: FWHM = 25 nm

Since the ionospheric photometer has a high sensitivity of about 226 counts/s/R at night, it is important to observe very weak ionospheric airglow at midnight and compensate for the lack of less global 135.6-nm airglow at midnight, especially for the middle and low latitude regions.

The GOLD ultraviolet imaging spectrograph is the payload of the SES-14 satellite in the geostationary orbit at the  $47.5^\circ$  W longitude. It observes approximately 18 h per day, including disk, limb, and stellar occultation observations, covering a variety of local times over the Americas. The GOLD has two identical imaging spectrometers covering bands of 132–162 nm with spectral resolutions of 0.2 nm for the daytime observation and 0.4 nm for the nighttime observation. For daytime scanning, the spatial grid is divided into  $125 \times 125$  km. Channel A observation is mainly used for daytime disk scanning, whereas channel B observation is used for night observation. From 20:10 to 22:55 universal time (UT), channel B images the hemisphere alternatively in 30 min periods (for example, 20:10 northern, 20:25 southern, 20:40 northern). Then, from 23:10 to 00:25 UT, both channel A and B work, each scanning one hemisphere in a temporal resolution of 15 min. The GOLD does not operate from approximately 00:30 to 06:10 UT. This paper includes more technical details on the GOLD instrument, operating schedule, and observations [37,38].

Due to its solar sun-synchronous orbit characteristics, the FY-3(D) IPM can continuously observe the ionospheric structure's variation with the longitude under the same local time. On the other hand, the GOLD is in geosynchronous orbit, which can continuously observe the same location and study the variation of the ionospheric structure over time.

Both were launched in recent years, and the data are new and of high quality. When studying the ionosphere at night, the data can corroborate one another.

### 3. Results

The FY-3(D) IPM nighttime data used in this paper are in the geomagnetic quiet period. We added all the 8 Kp values per day to obtain  $\Sigma Kp$  if  $\Sigma Kp < 20$  and every Kp  $< 5$ ; these data were used for the geomagnetic quiet period. The distribution of the OI135.6 nm radiation intensity at 02:00 LT in the geomagnetic quiet period was obtained using data from March 2019, as shown in Figure 1:

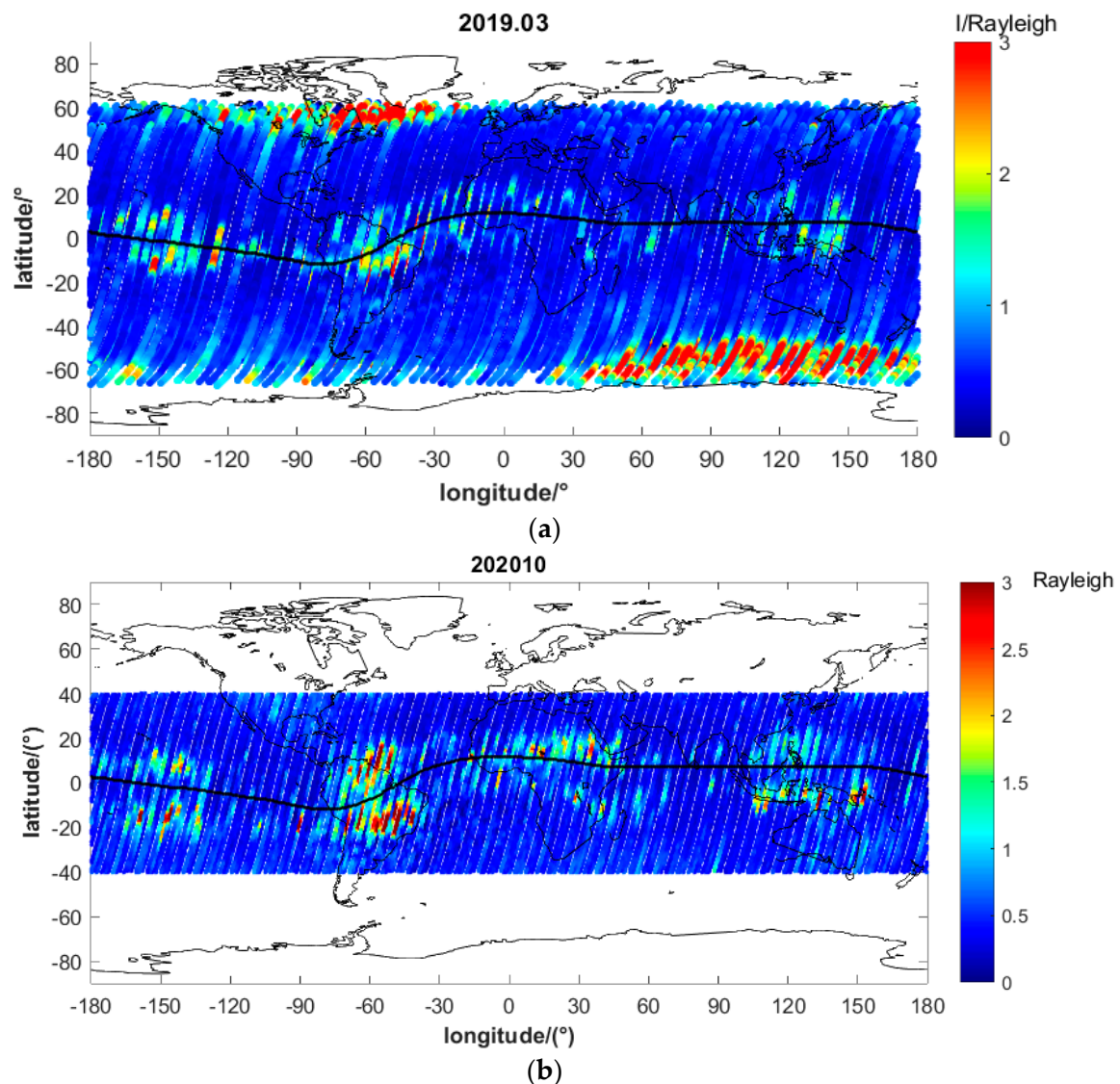


**Figure 1.** (a) FY-3(D) IPM observation of OI135.6 nm radiation intensity at 02:00 LT in March 2019. (b) FY-3(D) IPM observation of OI135.6 nm radiation intensity in low latitude at 02:00 LT in October 2020.

Figure 1a shows the global distribution of the OI135.6-nm nightglow intensity at 02:00 LT during the geomagnetic quiet period in March 2019. The horizontal axis is the longitude, the vertical axis is the latitude, and the color indicates the intensity. The black contour straddling in the middle of Figure 1a is the world map. The black line is the geomagnetic equator. In Figure 1a, two symmetrical high-intensity regions can be seen near 10° north and south of the geomagnetic equator, which embody the EIA in the intensity of the OI135.6 nm radiation band. The higher intensity in the high latitude is from auroras.

There are four intensity peaks at about  $-150^{\circ}$  W,  $-60^{\circ}$  W,  $30^{\circ}$  E, and  $120^{\circ}$  E in Figure 1b, and the EIA four-wave structure can still be clearly observed at 02:00 LT.

Figure 2 shows the global 135.6-nm nightglow at 2:00 LT in 2019.

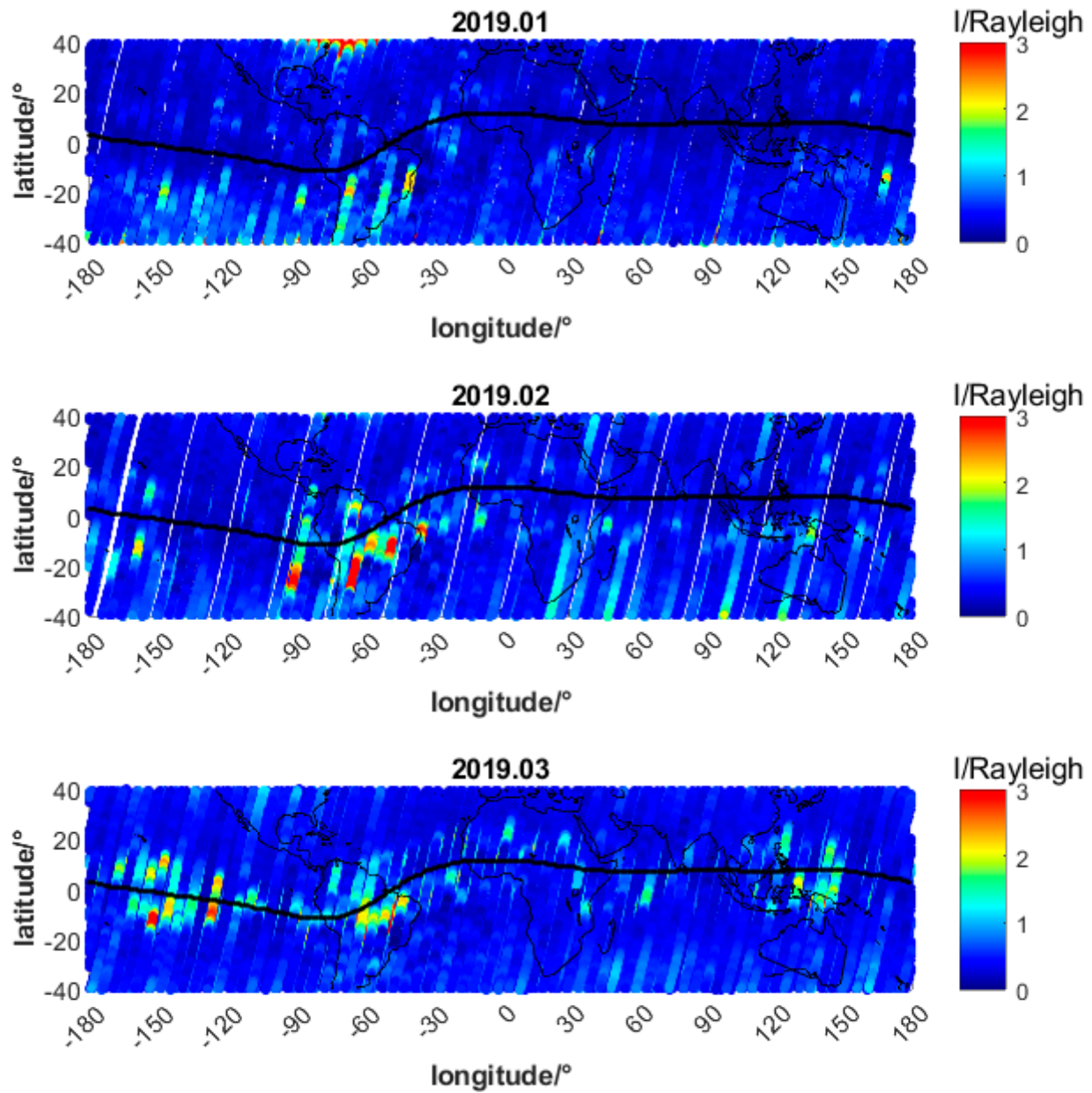


Figure 2. Cont.

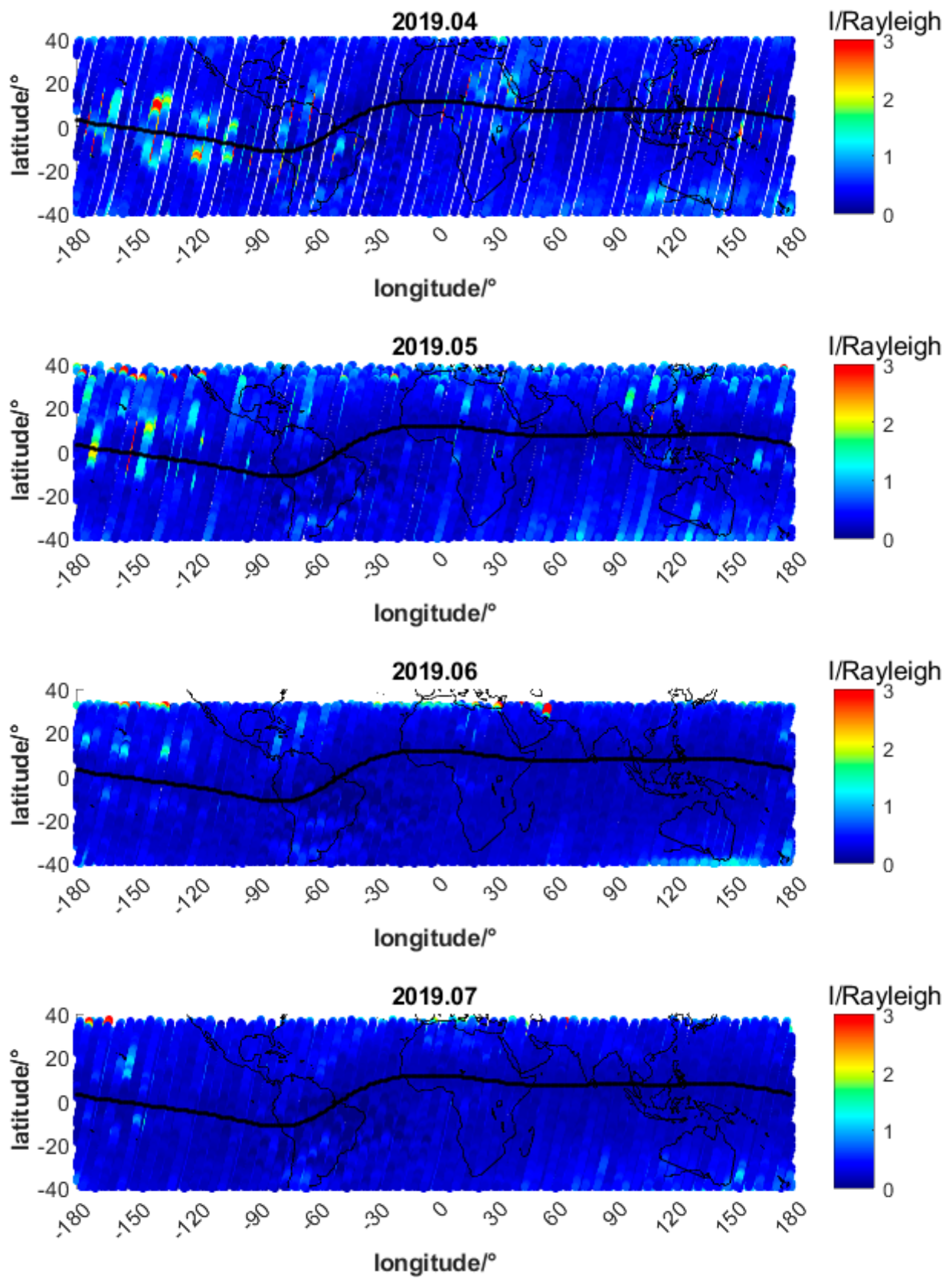


Figure 2. Cont.

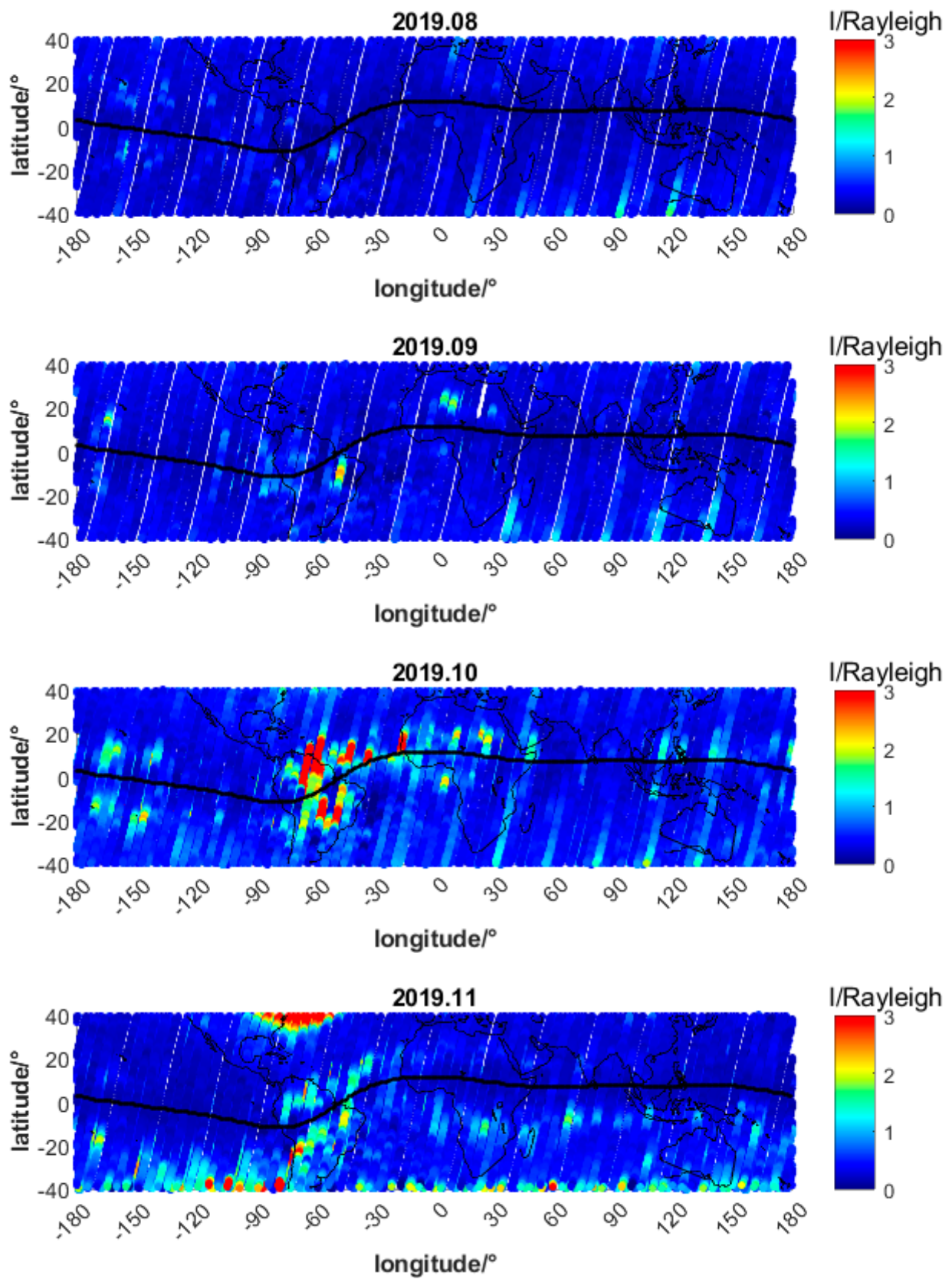
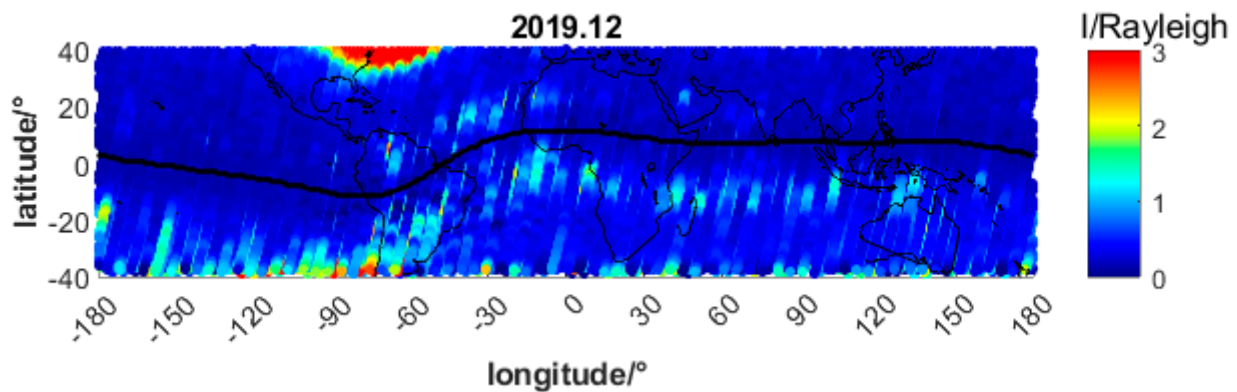


Figure 2. Cont.



**Figure 2.** Distribution of FY-3(D) IPMOI135.6 nm monthly radiation intensity at 02:00 LT in 2019 in low latitude.

In Figure 2, the EIA after midnight exists in many months, being the strongest in March, April, October, and November and weakest in June, July, and August, which has the same seasonal pattern as the EIA before midnight, being strong in equinoxes and weak in solstices.

Figure 3 shows the EIA variation in October and November from 2018 to 2020. Figure 3a,b show the EIA in October/November from 2018 to 2020. Figure 3c shows the variation between these two months. Figure 3d shows the monthly variation of the F10.7 index and EIA crest intensity from 2018 to 2020.

The upward plasma drift from the eastward electric and magnetic fields causes daytime EIA. Then, the plasma sinks along the magnetic field line to enhance the plasma concentration on both sides of the geomagnetic equator. After the disappearance of pre-reversal enhancement (PRE), the eastward electric field disappears, the upward drift ends, and the fountain effect cannot be maintained [39]. Related studies have shown that the EIA four-wave structure begins to form from 08:00 to 10:00 LT, becoming most significant from 12:00 to 16:00 LT, and decaying from 00:00 to 02:00 LT [26]. The EIA four-wave structure is visible in Figures 1 and 3a. Therefore, it can be assumed that the EIA after midnight is the residue of the EIA after the eastward electric field disappearance, and its intensity depends on the ionospheric activity before midnight. The F10.7 flux characterizes the solar EUV radiation level. The TEC intensity at the equator and low latitudes depends on the solar cycle, and the EIA is more obvious for  $F10.7 \geq 120$ , especially in the evening [31]. Therefore, studying the relationship between the EIA intensity and F10.7 flux after midnight can help us understand the existence of the EIA four-wave structure observed after midnight.

The region of  $-180^\circ$  to  $180^\circ$  longitude and  $-40^\circ$  to  $40^\circ$  latitude was divided into a grid of  $4 \times 4^\circ$ . Then, the FY-3(D) IPM data in the geomagnetic quiet period from October to November 2018, 2019, and 2020 were averaged in the grid separately. We obtained the distribution map of the OI135.6 nm radiation intensity in the grid for corresponding months. Figure 3a shows the intensity in October from 2018 to 2020. Figure 3b shows the intensity in November from 2018 to 2020. The high intensity at  $40^\circ$  N and  $70^\circ$  W, as shown in Figure 3b, is due to the influence of the aurora edge. Figure 3c shows the relative rate of the change in intensity, which is obtained from the following formula:

$$diff = \frac{I_{Nov} - I_{Oct}}{I_{Oct}} \times 100\% \quad (1)$$

where  $I_{Oct}$ ,  $I_{Nov}$  is the OI135.6 nm radiation intensity in October and November.

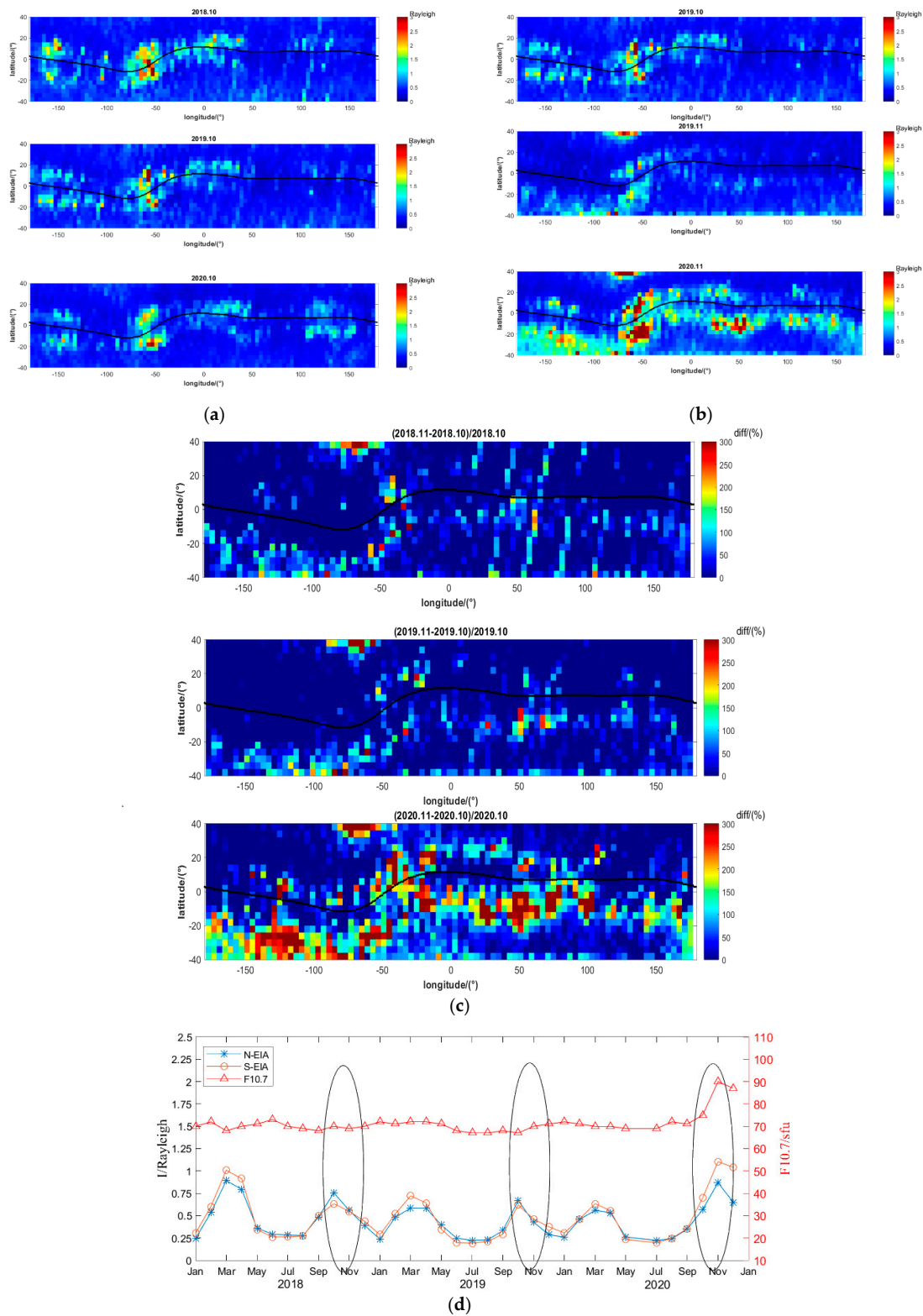


**Figure 3.** (a) FY-3(D) IPM OI135.6 nm radiation intensity in middle and low latitude at 02:00 LT in October from 2018 to 2020. (b) FY-3(D) IPM OI135.6 nm radiation intensity in middle and low latitude at 02:00 LT in November from 2018 to 2020. (c) The relative change of FY-3(D) IPM OI135.6 nm radiation intensity in middle and low latitude in November versus October from 2018 to 2020. (d) The F10.7 index and EIA crest intensity monthly variation from 2018 to 2020. The red line is the F10.7 index monthly variation. The blue line and gray line show the monthly variation of the north and south EIA crest intensity, respectively.

In Figure 3b,c, the OI135.6 nm radiation intensity observed by the FY-3(D) in November 2020 was significantly enhanced compared to last month and the same month of previous years.

Figure 3c shows that, within the EIA structure, the OI135.6 nm radiation intensity in November 2018 and 2019 has a relative increase and decrease. However, in November 2020, the OI135.6 nm radiant intensity increased with a relative change rate of about 100–200%. The relative change rate of the OI135.6 nm radiation intensity in November 2020 was significantly enhanced compared with November 2018 and 2019.

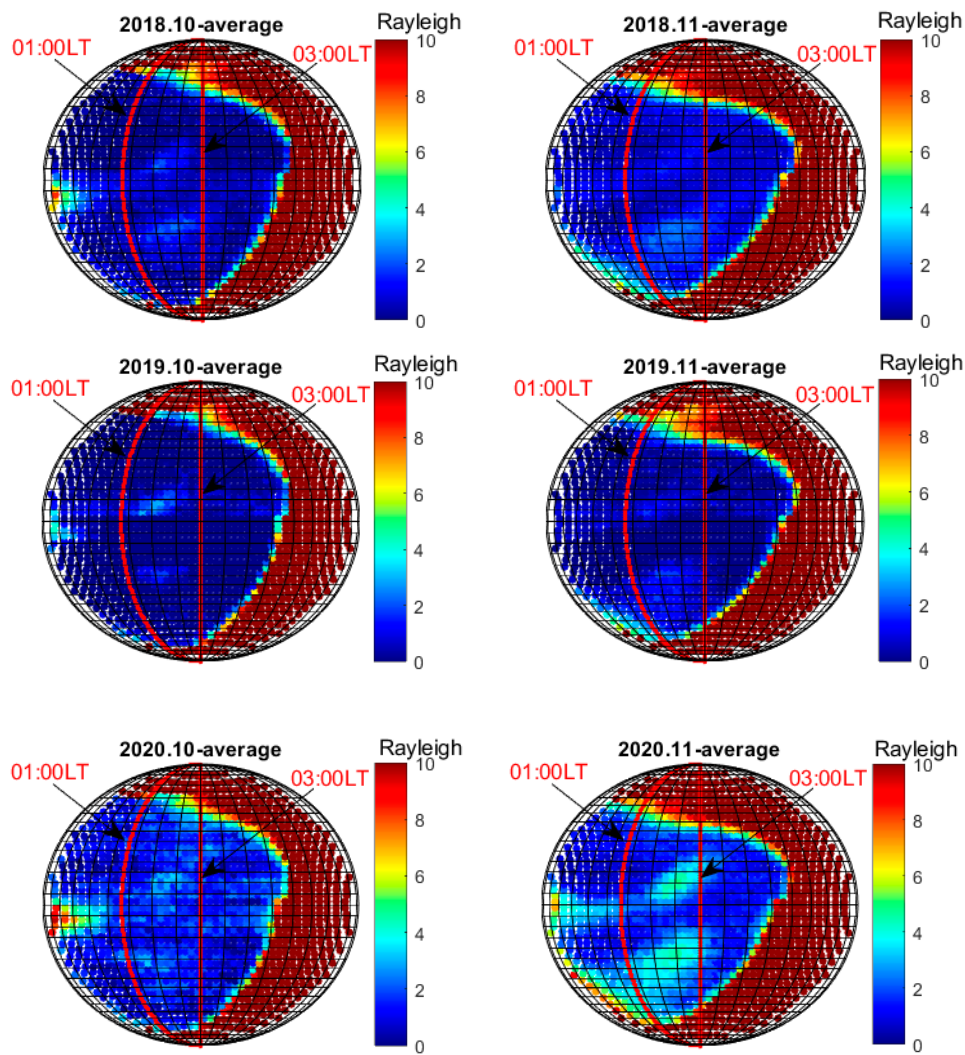
The red line in Figure 3d shows the F10.7 index variation from 2018 to 2021. The electron density has a peak region between the magnetic latitudes  $10^{\circ}$ – $15^{\circ}$  in the daytime due to the ionospheric fountain effect. In the nighttime, the high-density region in the low latitudes moves equatorward. Therefore, the peaked structure along the magnetic latitude will be smaller after midnight [40]. Li et al. found that the location of the EIA crests moved poleward during high solar activity periods relative to that during low solar activity, because of the enhanced  $E \times B$  force [41]. The years of data we used in this paper are in the comparatively low solar activity periods. Therefore, we selected the geomagnetic latitude  $\pm 10^{\circ}$  as the location of the north or south EIA crest, and the averaged EIA crest intensity per month was obtained by averaging along the longitude. The blue and gray lines in Figure 3d show the north and south EIA intensity, respectively. The solar cycle has entered an ascending phase since November 2020 (actually F10.7 totally increased after September 2021), and the averaged north and south EIA crest intensity have also increased with the gradual increase in the solar activity. During the month of the F10.7 enhancement, the ionosphere becomes more active and the EIA becomes stronger during the daytime, resulting in a strong EIA in the ionosphere at 02:00 LT. As shown in the ellipse in Figure 3d, the extreme value of the EIA crest occurred in October from 2018 to 2019. However, in 2020, the extreme value of the EIA crest occurred in November, indicating that the EIA crest intensity after midnight positively responded to the solar activity.

Figure 4 shows the averaged EIA in October and November from 2018 to 2020 using the GOLD data. Our results show nearly the same variation as the data from the IPM.

The averaged 135.6 nm nightglow intensity of the GOLD at 06:10 UT (scanning the northern hemisphere), and 06:22 UT (scanning the southern hemisphere) in October and November from 2018 to 2020 was also obtained, as shown in Figure 3d. The red line on the left is the longitude line corresponding to 01:00 LT and the red line on the right is the longitude line corresponding to 03:00 LT. In Figure 4, the OI135.6 nm averaged radiation intensity observed by the GOLD in November 2020 from 01:00 to 03:00 LT was also significantly enhanced compared to last month and the same period of the previous year. The FY-3(D) IPM and the GOLD showed a positive correlation between the ionospheric response and the solar activity enhancement after midnight. Figures 3c and 4 both show that the spatial distribution pattern of the region with a significant relative change rate of the OI135.6 nm radiation intensity is consistent with the spatial distribution pattern of the EIA. In regions outside the EIA, the intensity did not change.

Some studies found that the latitudes of the EIA crest moved poleward with the enhancement of the solar activity [41–43]. However, no study focuses on the monthly variation of the  $\theta_{ml}F2$  at the same local time after midnight. Figure 5 shows the  $\theta_{ml}F2$  monthly variation in both the northern and southern hemisphere from 2018 to 2021.

The magnetic latitude of the peak OI135.6 nm intensity was selected in the north and south of the geomagnetic equator, and the monthly average value was obtained. The blue line is the monthly change curve of the  $\theta_{ml}F2$  in the northern hemisphere and the brown line is the monthly change curve of the  $\theta_{ml}F2$  in the southern hemisphere. For some reason, satellite data in June 2020 are missing.



**Figure 4.** The GOLD averaged radiation intensity at OI135.6 nm in October and November at midnight from 2018 to 2020. The two red lines in the figure are the longitude lines corresponding to 01:00 and 03:00 LT from left to right, respectively.

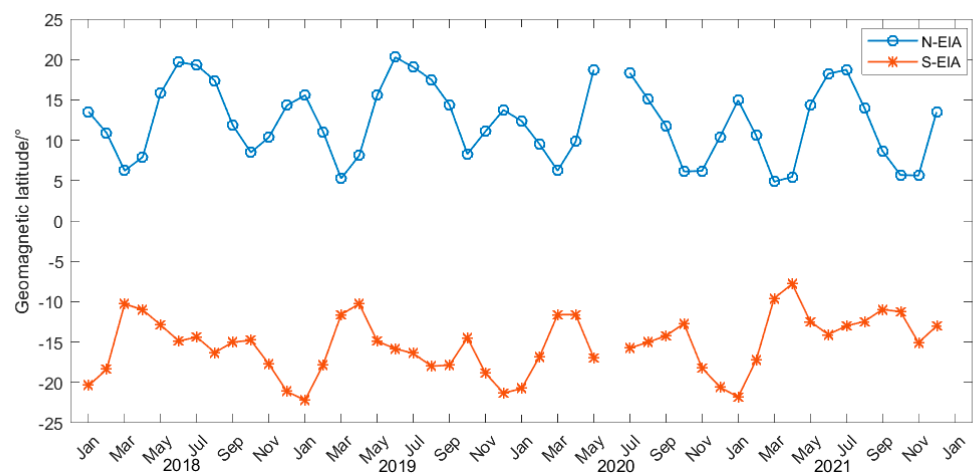


**Figure 5.** Monthly variation of  $\theta_{mI} F2$  from 2018 to 2021.

The figure shows that the  $\theta_{ml}F2$  in the northern and southern hemispheres has an annual cycle. The EIA crests are closer to the geomagnetic equator in equinoxes, while they are farther away from that in solstices. The  $\theta_{ml}F2$  reach the maximum peak in the hemisphere summer and the secondary peak in the hemisphere winter. In addition, the  $\theta_{ml}F2$  in the northern hemisphere has a greater annual variation, ranging from about  $5^\circ$  to  $20^\circ$ , while that ranges from about  $-20^\circ$  to  $-10^\circ$  in the southern hemisphere.

Previous research mainly studied the influence of the solar activity on the  $\theta_{ml}F2$ , without focusing on the monthly variation [41]. Our results are not consistent with the findings of Huang et al. [43]. On the one hand, it is because they studied the daytime  $\theta_{ml}F2$ , and we studied the nighttime  $\theta_{ml}F2$ . On the other hand, they were not fixed on the local time, and the  $\theta_{ml}F2$  itself will change with the local time, which will cause errors in their results. Furthermore, the hemispherically asymmetric range of the  $\theta_{ml}F2$  within a year is shown in this article.

#### 4. Conclusions

Based on the OI135.6 nm intensity data detected by the Ionospheric Photometer (IPM) on the FY-3(D) satellite, we studied the seasonal variation of the EIA in the low latitudes around 02:00 LT in the geomagnetic quiet period. The EIA still exists at 02:00 LT after midnight in low solar activity years, and the four-wave structure can still be observed in certain months (especially in March and October). We also found a positive correlation between the EIA four-wave structure at 02:00 LT and the solar activity. The EIA at 02:00 LT has the same seasonal pattern as the EIA before midnight: strong in equinoxes and weak in solstices. In 2020, the F10.7 index increased from 75 sfu in October to 90 sfu in November. At the same time, the OI135.6 nm intensity in the EIA region increased by 100–200% compared with last month, which was higher than the same period in the previous two years. Meanwhile, we used the GOLD data and found a stronger EIA from 01:00 to 03:00 LT as the solar activity increased, which had a good consistency with the FY-3(D) IPM data. Considering that the F10.7 enhancement represents the increase in the solar radiation level, the plasma density of the whole ionosphere increases during the daytime, and the EIA is enhanced. The  $E \times B$  drift could not be maintained to transport plasma to higher altitudes due to the disappearance of the eastward electric field, and the EIA began to decay at local time. The enhanced ionospheric plasma density during the daytime could maintain a stronger EIA after midnight. Therefore, the EIA at 02:00 LT after midnight can be considered the residue of the EIA before the midnight attenuation.

We also studied the  $\theta_{ml}F2$  monthly variation in both the northern and southern hemispheres at 02:00 LT during 2018 to 2021 and found that the hemispherically asymmetric range of the  $\theta_{ml}F2$ , which is wider in the southern hemisphere and narrower in the southern hemisphere. Within a year, the EIA crest is closer to the geomagnetic equator in equinoxes and farther away from the geomagnetic equator in solstices. The principle behind these results still needs further studies.

**Author Contributions:** Conceptualization, L.F., T.W., R.P. and T.M.; Formal analysis, B.Z. and F.J.; Investigation, all authors; Data curation, T.M., X.H. and J.W.; Writing—original draft, B.Z.; Writing—review & editing, L.F., T.M. and J.W.; Visualization, B.Z.; Supervision, L.F., N.J., T.W. and R.P.; Project administration, L.F., T.M. and X.H.; Funding acquisition, L.F. and T.M. All authors have read and agreed to the published version of the manuscript.

**Funding:** This study was supported by the National Natural Science Foundation of China (NO. 42174226, 41874187).

**Data Availability Statement:** The source of the Kp index data used in this article is <https://wdc.kugi.kyoto-u.ac.jp/kp/index.html#LIST/> (accessed on 27 October 2022). The FY-3(D) data are from <https://satellite.nsmc.org.cn/portalsite/default.aspx/> (accessed on 27 October 2022). F10.7 Flux data sources: [ftp://ftp.swpc.noaa.gov/pub/indices/old\\_indices/](ftp://ftp.swpc.noaa.gov/pub/indices/old_indices/) (accessed on 22 April 2022). A brief introduction to the F10.7 index can be found in this paper. GOLD L1D data source: <https://gold.cs.ucf.edu/data/search/> (accessed on 14 November 2022).

**Conflicts of Interest:** The authors declare no conflict of interest.

## References

1. Anderson, D.N. A theoretical study of the ionospheric *F* region equatorial anomaly-I. Theory. *Planet. Space Sci.* **1973**, *21*, 409–419. [[CrossRef](#)]
2. Duncan, R.A. The Equatorial *F*-region of the Ionosphere. *J. Atmos. Sol. Terr. Phys.* **1960**, *18*, 89–100. [[CrossRef](#)]
3. Rishbeth, H. Polarization Fields Produced by Winds in the Equatorial *F* Region. *Planet. Space Sci.* **1971**, *19*, 357–369. [[CrossRef](#)]
4. Martyn, D.F. Atmospheric Tides in the Ionosphere—I. Solar Tides in the *F2* Region. *Proc. R. Soc. Lond. Ser. A* **1947**, *189*, 241–260. [[CrossRef](#)]
5. Croom, S.; Robbins, A.; Thoma, J.O. Two Anomalies in the Behavior of the *F2* Layer of the Ionosphere. *Nature* **1959**, *184*, 2003–2004. [[CrossRef](#)]
6. Meier, R.R. Ultraviolet Spectroscopy and Remote Sensing of the Upper Atmosphere. *Space Sci. Rev.* **1991**, *58*, 1–185. [[CrossRef](#)]
7. Kamalabadi, F.; Karl, W.C.; Semeter, J.L.; Cotton, D.M.; Cook, T.A.; Chakrabarti, S. A Statistical Framework for Space-Based EUV Ionospheric Tomography. *Radio Sci.* **1999**, *34*, 437–447. [[CrossRef](#)]
8. Dymond, K.F.; Thonnard, S.E.; McCoy, R.P.; Thomas, R.J. An Optical Remote Sensing Technique for Determining Nighttime *F* Region Electron Density. *Radio Sci.* **1997**, *32*, 1985–1996. [[CrossRef](#)]
9. Kil, H.; DeMajistre, R.; Paxton, L.J. *F*-Region Plasma Distribution Seen from TIMED/GUVI and Its Relation to the Equatorial Spread *F* Activity: *F*-Region Plasma Density from TIMED/GUVI. *Geophys. Res. Lett.* **2004**, *31*. [[CrossRef](#)]
10. Paxton, L.J.; Christensen, A.B.; Humm, D.C.; Ogorzalek, B.S.; Pardoe, C.T.; Morrison, D.; Weiss, M.B.; Crain, W.; Lew, P.H.; Mabry, D.J.; et al. Global Ultraviolet Imager (GUVI): Measuring Composition and Energy Inputs for the NASA Thermosphere Ionosphere Mesosphere Energetics and Dynamics (TIMED) Mission. In Proceedings of the Proceedings Optical Spectroscopic Techniques and Instrumentation for Atmospheric and Space Research III, Denver, CO, USA, 20 October 1999; p. 265.
11. Christensen, A.B. Initial Observations with the Global Ultraviolet Imager (GUVI) in the NASA TIMED Satellite Mission. *J. Geophys. Res.* **2003**, *108*, 1451. [[CrossRef](#)]
12. Rajesh, P.K.; Liu, J.Y.; Hsu, M.L.; Lin, C.H.; Oyama, K.I.; Paxton, L.J. Ionospheric Electron Content and NmF2 from Nighttime OI 135.6 Nm Intensity: IEC and NMF2 USING OI 135.6 NM INTENSITY. *J. Geophys. Res. Space Phys.* **2011**, *116*. [[CrossRef](#)]
13. Jiang, F.; Mao, T.; Zhang, X.; Wang, Y.-G.; Hu, X.; Wang, D.; Jia, N.; Wang, T.; Sun, Y.; Fu, L.-P. Observation of Thermosphere and Ionosphere Using the Ionosphere PhotoMeter (IPM) on the Chinese Meteorological Satellite FY-3D. *Adv. Space Res.* **2020**, *66*, 2151–2167. [[CrossRef](#)]
14. Meier, R.R.; Picone, J.M.; Drob, D.; Bishop, J.; Emmert, J.T.; Lean, J.L.; Stephan, A.W.; Strickland, D.J.; Christensen, A.B.; Paxton, L.J.; et al. Remote Sensing of Earth's Limb by TIMED/GUVI: Retrieval of Thermospheric Composition and Temperature. *Earth Space Sci.* **2015**, *2*, 1–37. [[CrossRef](#)]
15. DeMajistre, R. Retrievals of Nighttime Electron Density from Thermosphere Ionosphere Mesosphere Energetics and Dynamics (TIMED) Mission Global Ultraviolet Imager (GUVI) Measurements. *J. Geophys. Res.* **2004**, *109*, A05305. [[CrossRef](#)]
16. Kamalabadi, F.; Bust, G.; Dymond, K.; Gonzalez, S.; Bernhardt, P.; Chakrabarti, S.; Cotton, D.; Stephan, A.; McCoy, R.; Budzien, S.; et al. Tomographic Studies of Aeronomic Phenomena Using Radio and UV Techniques. *J. Atmospheric Sol. Terr. Phys.* **2002**, *64*, 1573–1580. [[CrossRef](#)]
17. Balan, N.; Souza, J.; Bailey, G.J. Recent Developments in the Understanding of Equatorial Ionization Anomaly: A Review. *J. Atmospheric Sol. Terr. Phys.* **2018**, *171*, 3–11. [[CrossRef](#)]
18. Cai, X.; Burns, A.G.; Wang, W.; Coster, A.; Qian, L.; Liu, J.; Solomon, S.C.; Eastes, R.W.; Daniell, R.E.; McClintock, W.E. Comparison of GOLD Nighttime Measurements With Total Electron Content: Preliminary Results. *J. Geophys. Res. Space Phys.* **2020**, *125*, e2019JA027767. [[CrossRef](#)]
19. Sagawa, E.; Maruyama, T.; Immel, T.J.; Frey, H.U.; Mende, S.B. Global View of the Nighttime Low-Latitude Ionosphere by the IMAGE/FUV 135.6 Nm Observations: Global view of the Equatorial Ionosphere. *Geophys. Res. Lett.* **2003**, *30*. [[CrossRef](#)]
20. Barth, C.A.; Schaffner, S. OGO 4 Spectrometer Measurements of the Tropical Ultraviolet Airglow. *J. Geophys. Res.* **1970**, *75*, 4299–4306. [[CrossRef](#)]
21. Rodríguez-Zuluaga, J.; Stolle, C.; Yamazaki, Y.; Xiong, C.; England, S.L. A Synoptic-Scale Wavelike Structure in the Nighttime Equatorial Ionization Anomaly. *Earth Space Sci.* **2021**, *8*, e2020EA001529. [[CrossRef](#)]
22. Sagawa, E.; Immel, T.J.; Frey, H.U.; Mende, S.B. Longitudinal Structure of the Equatorial Anomaly in the Nighttime Ionosphere Observed by IMAGE/FUV. *J. Geophys. Res.* **2005**, *110*, A11302. [[CrossRef](#)]
23. Liu, J.; Liu, L.; Zhao, B.; Lei, J.; Wan, W. On the Relationship between the Postmidnight Thermospheric Equatorial Mass Anomaly and Equatorial Ionization Anomaly under Geomagnetic Quiet Conditions: BRIEF REPORT. *J. Geophys. Res. Space Phys.* **2011**, *116*. [[CrossRef](#)]
24. Kil, H.; DeMajistre, R.; Paxton, L.J.; Zhang, Y. Nighttime-Region Morphology in the Low and Middle Latitudes Seen from DMSP F15 and TIMED/GUVI. *J. Atmospheric Sol. Terr. Phys.* **2006**, *68*, 1672–1681. [[CrossRef](#)]
25. Henderson, S.B.; Swenson, C.M.; Christensen, A.B.; Paxton, L.J. Morphology of the Equatorial Anomaly and Equatorial Plasma Bubbles Using Image Subspace Analysis of Global Ultraviolet Imager Data. *J. Geophys. Res.* **2005**, *110*, A11306. [[CrossRef](#)]
26. Lin, C.H.; Hsiao, C.C.; Liu, J.Y.; Liu, C.H. Longitudinal Structure of the Equatorial Ionosphere: Time Evolution of the Four-Peaked EIA Structure: LONGITUDINAL EIA STRUCTURE. *J. Geophys. Res. Space Phys.* **2007**, *112*, e2007JA012455. [[CrossRef](#)]

27. Lin, C.H.; Liu, J.Y.; Fang, T.W.; Chang, P.Y.; Tsai, H.F.; Chen, C.H.; Hsiao, C.C. Motions of the Equatorial Ionization Anomaly Crests Imaged by FORMOSAT-3/COSMIC. *Geophys. Res. Lett.* **2007**, *34*, L19101. [[CrossRef](#)]
28. Laskar, F.I.; Eastes, R.W.; Martinis, C.R.; Daniell, R.E.; Pedatella, N.M.; Burns, A.G.; McClintock, W.; Goncharenko, L.P.; Coster, A.; Milla, M.A.; et al. Early Morning Equatorial Ionization Anomaly From GOLD Observations. *J. Geophys. Res. Space Phys.* **2020**, *125*, e2019JA027487. [[CrossRef](#)]
29. Cai, X.; Qian, L.; Wang, W.; McNerney, J.M.; Liu, H.; Eastes, R.W. Investigation of the Post-Sunset Extra Electron Density Peak Poleward of the Equatorial Ionization Anomaly Southern Crest. *J. Geophys. Res. Space Phys.* **2022**, *127*, e2022JA030755. [[CrossRef](#)]
30. Cai, X.; Qian, L.; Wang, W.; McNerney, J.M.; Liu, H.; Eastes, R.W. Hemispherically Asymmetric Evolution of Nighttime Ionospheric Equatorial Ionization Anomaly in the American Longitude Sector. *J. Geophys. Res. Space Phys.* **2022**, *127*, e2022JA030706. [[CrossRef](#)]
31. Jee, G. Analysis of TEC Data from the TOPEX/Poseidon Mission. *J. Geophys. Res.* **2004**, *109*, A01301. [[CrossRef](#)]
32. Immel, T.J.; Sagawa, E.; England, S.L.; Henderson, S.B.; Hagan, M.E.; Mende, S.B.; Frey, H.U.; Swenson, C.M.; Paxton, L.J. Control of Equatorial Ionospheric Morphology by Atmospheric Tides. *Geophys. Res. Lett.* **2006**, *33*, L15108. [[CrossRef](#)]
33. Guo, B.; Xu, J.; Sun, L.; Lin, Y.; Yuan, W. The Seasonal and Longitudinal Variations of Nighttime OI 135.6-nm Emission at Equatorial Ionization Anomaly Crests Observed by the DMSP/SSUSI. *J. Geophys. Res. Space Phys.* **2020**, *125*, e2019JA027764. [[CrossRef](#)]
34. Wang, Y.; Fu, L.; Jiang, F.; Hu, X.; Liu, C.; Zhang, X.; Li, J.; Ren, Z.; He, F.; Sun, L.; et al. Far-ultraviolet airglow remote sensing measurements on Feng Yun 3-D meteorological satellite. *Atmos. Meas. Tech.* **2022**, *15*, 1577–1586. [[CrossRef](#)]
35. Jiang, F.; Mao, T.; Zhang, X.; Wang, Y.; Fu, L.; Hu, X.; Wang, D.; Jia, N.; Wang, T.; Sun, Y. The Day-Glow Data Application of FY-3D IPM in Monitoring O/N<sub>2</sub>. *J. Atmospheric Sol. Terr. Phys.* **2020**, *205*, 105309. [[CrossRef](#)]
36. Wang, D.; Fu, L.; Jiang, F.; Jia, N.; Wang, T.; Dou, S. Inversion of Ionospheric O/N<sub>2</sub> by Using FY-3D Ionospheric Photometer Data. *Spectrosc. Spectr. Anal.* **2021**, *41*, 1004–1010. [[CrossRef](#)]
37. Eastes, R.W.; McClintock, W.E.; Burns, A.G.; Anderson, D.N.; Andersson, L.; Codrescu, M.; Correira, J.T.; Daniell, R.E.; England, S.L.; Evans, J.S.; et al. The Global-Scale Observations of the Limb and Disk (GOLD) Mission. *Space Sci. Rev.* **2017**, *212*, 383–408. [[CrossRef](#)]
38. Eastes, R.W.; McClintock, W.E.; Burns, A.G.; Anderson, D.N.; Andersson, L.; Aryal, S.; Budzien, S.A.; Cai, X.; Codrescu, M.V.; Correira, J.T.; et al. Initial Observations by the GOLD Mission. *J. Geophys. Res. Space Phys.* **2020**, *125*, e2020JA027823. [[CrossRef](#)]
39. Greer, K.R.; Eastes, R.; Solomon, S.; McClintock, W.; Burns, A.; Rusch, D. Variations of Lower Thermospheric FUV Emissions Based on GOLD Observations and GLOW Modeling. *J. Geophys. Res. Space Phys.* **2020**, *125*, e2020JA027810. [[CrossRef](#)]
40. Tsai, T.C.; Jhuang, H.K.; Lee, L.C.; Ho, Y.Y. Ionospheric Peaked Structures and Their Local Time, Seasonal, and Solar Activity Dependence Based on Global Ionosphere Maps. *J. Geophys. Res. Space Phys.* **2019**, *124*, 7994–8014. [[CrossRef](#)]
41. Li, K.-F.; Lin, L.-C.; Bui, X.-H.; Liang, M.-C. The 11 Year Solar Cycle Response of the Equatorial Ionization Anomaly Observed by GPS Radio Occultation. *J. Geophys. Res.* **2018**, *123*, 848–861. [[CrossRef](#)]
42. Kumar, S.; Singh, A.K.; Lee, J. Equatorial Ionospheric Anomaly (EIA) and Comparison with IRI Model during Descending Phase of Solar Activity (2005–2009). *Adv. Space Res.* **2014**, *53*, 724–733. [[CrossRef](#)]
43. Huang, Y.-N.; Cheng, K. Solar Cycle Variations of the Equatorial Ionospheric Anomaly in Total Electron Content in the Asian Region. *J. Geophys. Res. Space Phys.* **1996**, *101*, 24513–24520. [[CrossRef](#)]